Chapter – 5

Simultaneous adsorption of organic pollutants on Mo-doped $NiFe_2O_4$ nanoparticles: Experimental and computational studies

5.1 Introduction

Adsorption is an economical and efficient technology for removing (or separating) water-soluble toxic organic chemicals from an aqueous medium[12]. As we discovered in Chapter 4, nickel ferrite exhibits exceptional superparamagnetic properties. So, it can be separated from water by applying an external magnetic field. These particles can be re-dispersed in water by simple bath sonication or stirring. The combination of magnetic decantation and easy re-dispersal avoids the need for complex separation systems. It also possesses excellent stability and chemical durability, ensuring long-lasting performance and reusability for multiple cycles of pollutant removal. However, the adsorption properties reported for pristine $NiFe_2O_4$ are mostly insignificant. For example, Jiang et al. reported weak adsorption of methyl orange (MG) dye on pure $NiFe_2O_4$ particles. In contrast, the composites of $NiFe_2O_4$ with activated carbon (AC) and carbon dots have demonstrated appreciable removal of the target organic pollutant in 30 minutes[40,206]. Nevertheless, the disadvantage of such composites is that the $NiFe_2O_4$ part contributes very little to adsorption of the target organic pollutant. Its role is mostly confined to facilitating easy magnetic separation part of the adsorbent. Considerable enhancement in adsorption properties may be achieved if the $NiFe_2O_4$ part also contributes appreciably to the removal of the organic pollutants.

Doping of foreign elements into the crystal structure of $NiFe_2O_4$ can modify its electronic structure, create additional binding sites, and enhance adsorption affinity for specific pollutants [207]. In addition, doping in nickel ferrite may also increase its surface area and porosity[207]. For instance, Luo et al. synthesized Mn-doped $NiFe_2O_4$ by the hydrothermal method and observed 231.74 mg g^{-1} adsorption capacity for Congo red adsorption [208]. Sulaiman et al. showed that Al-doped $NiFe_2O_4$, obtained by a modified sol-gel approach, had an adsorption capacity of 28.71 mg g^{-1} for CO_2 gas [209]. Kumari et al.

synthesized the alkaline earth metal doped $NiFe_2O_4$ by co-precipitation method and compared the adsorption efficiency of pure and doped $NiFe_2O_4$. They found 83% and 45% removal of Pb (II) and Cd (II) ions utilizing pure nickel ferrite nano adsorbents. The removal levels reached 97% and 80% for alkaline earth metal doped nickel ferrite nanoparticles[210].

The foregoing literature survey shows that there are only a few investigations on the adsorption properties of metal ion-doped $NiFe_2O_4$ nanoparticles. Moreover, such doping can also result in different types of sites on the doped $NiFe_2O_4$ surface [211]. Efficient concurrent co-adsorption of two organic pollutants could be envisaged on such adsorbent surfaces[82,201]. From this perspective, the transition element molybdenum (Mo) is an attractive candidate as a dopant [212,213]. It has higher electronegativity than Ni or Fe, which can affect electron distribution and result in different types of adsorption sites. Mo has various oxidation states and can take up a tetrahedral or an octahedral site in the $NiFe_2O_4$ crystal lattice. Note that the synthesis and characterization of Mo-doped $NiFe_2O_4$ nanoparticles have not been reported earlier in the literature. Consequently, there are no investigations on the adsorption properties of Mo-doped $NiFe_2O_4$ nanoparticles.

Given the possibility of the formation of different types of adsorption sites, the present chapter investigates the co-adsorption or simultaneous removal of two organic pollutants, methyl orange (MG) and ciprofloxacin (CIP), by Mo-doped $NiFe_2O_4$ nanoparticles. MG and CIP are large organic molecules that have two or more sites through which they can adsorb to the adsorbent. Naturally, adsorbents with different types of sites can exhibit efficient co-adsorption of two organic molecules. For example, the previous chapter showed that the $NiFe_2O_4$/GO composite could co-adsorb MG and CIP from a dilute aqueous solution of both[82].

In this chapter, Mo-doped $NiFe_2O_4$ nanoparticles with different percentages of Mo-doping were synthesized by one step-hydrothermal method. A variety of analytical techniques were employed to examine the Mo-doped $NiFe_2O_4$ samples. Batch adsorption studies were carried out to evaluate the adsorption capacity and cycle performance of the prepared Mo-doped $NiFe_2O_4$ particles. Equilibrium adsorption data have been fitted to different extended adsorption isotherm equations. Nevertheless, it is difficult to get any molecular-level understanding of interactions between different adsorbent and adsorbate sites from adsorption isotherms. The situation becomes more complicated when dealing with a co-adsorption problem. Hence, DFT calculations were also conducted to investigate adsorbent-adsorbate(s) interactions. A combination of experimental and DFT calculation results helped elucidate the molecular-level adsorption mechanism.

5.2 Experimental section

5.2.1 Hydrothermal synthesis of Mo-doped $NiFe_2O_4$ nanoparticles

The first step was mixing 0.0022 g of $(NH_4)_6Mo_7O_{24}.4H_2O$ (Merck) and 1.005 g of $Fe(NO_3)_3.9H_2O$ in 40 ml of DW with continuous stirring for an hour. This mixture was treated with 0.3635 g $Ni(NO_3)_2.6H_2O$ salt. Next, 1M NaOH was added dropwise to the aforesaid reaction mixture until the pH reached 12. The reaction mixture was stirred for three more hours until a brown precipitate appeared. At this stage, this mixture was transferred into an autoclave and treated at 180°C for 24 hours. The resulting dark brown precipitate was carefully washed with distilled water and ethanol and then dried at 70°C in an oven. The procedure mentioned above outlines the synthesis of 1% Mo-doped $NiFe_2O_4$ nanoparticles. The 2% and 4% Mo-doped $NiFe_2O_4$ nanoparticles were prepared similarly, the only difference being the amount of $(NH_4)_6Mo_7O_{24}.4H_2O$ utilized in the synthesis. The synthesized Mo-doped $NiFe_2O_4$ samples were abbreviated as 1MNIF, 2MNIF, and 4MNIF.

Here 1, 2, and 4 correspond to atomic percent (at%) Mo-dopant in $NiFe_2O_4$, respectively. Pure $NiFe_2O_4$ was prepared using an analogous protocol without adding $(NH_4)_6Mo_7O_{24}.4H_2O$ salt.

5.2.2 Adsorption experiments

Adsorption experiments were conducted for single and binary adsorbate systems. The adsorption experiment's procedure is the same as discussed in Chapter 4. Adsorption experiments were conducted with different adsorbent doses to obtain the optimized adsorbent dose for a given adsorbate concentration. All adsorption experiments were, therefore, conducted with the optimized adsorbent dose (10 mg in 20 ml) found by this range of experiments. Adsorption experiments were also carried out at different pH values ranging from 2-12 to determine the optimum pH for adsorption. The CIP or MG aqueous solution was treated with 0.1M HCl or 0.1M NaOH to achieve the required pH. The equilibrium adsorption isotherm data were collected from adsorption experiments with binary solutes containing equal volumes (10 ml each) of CIP (12-48 mg L^{-1}) and MG (4-16 mg L^{-1}) aqueous solutions. The adsorption capacity and percentage removal efficiency were calculated by the equations (1.1), (1.2), and (1.3) given in Chapter 1 of this thesis.

5.2.3 Plane-wave DFT modeling and methodology

Plane-wave DFT calculations were performed to locate the Mo dopant position in $NiFe_2O_4$ crystal on the MedeA VASP (Vienna ab initio simulation package) software (Version 5.4.4). The calculations used generalized gradient approximation Perdew–Burke–Ernzerhoff (GGA-PBE) exchange-correlation functional [214] and the projector augmented wave (PAW) pseudopotentials. The 56-atom unit cell of the FCC inverse spinel $NiFe_2O_4$ (MP-22684)[215] was optimized using 2 × 2 × 2 k-points and 550 eV energy cut-off. The magnetic effects of $NiFe_2O_4$ were taken into consideration by using spin-polarized calculations. The optimized unit cell is labeled as N0 in the rest of the manuscript (Figures 5.1a and 5.1b). The four

different Mo-substituted $NiFe_2O_4$ models were built in which the dopant substitutes different sites (Figure 5.2 (a-d)). The models have the dopant Mo atom substituting (1) the octahedral Fe (denoted by N1), (2) the tetrahedral Fe (denoted by N2), (3) the octahedral Ni (denoted by N3), and (4) occupying an interstitial position (denoted by N4) in the optimized $NiFe_2O_4$ lattice (N0 model). These four models were optimized with the same calculation parameters as mentioned above. The convergence criteria for structure optimization were set to (1) energy tolerance of 1.0×10^{-5} eV and (2) maximum force tolerance of 0.02 eV. The formation energies of the four doped systems were calculated using the following equations.

$$E_f = E_{defect}(N_1) - (E_{perfect}(NiFe_2O_4) - \mu_{Fe} + \mu_{Mo}) \quad (5.1)$$

$$E_f = E_{defect}(N_2) - \left(E_{perfect}(NiFe_2O_4) - \mu_{Fe} + \mu_{Mo}\right) \quad (5.2)$$

$$E_f = E_{defect}(N_3) - (E_{perfect}(NiFe_2O_4) - \mu_{Ni} + \mu_{Mo}) \quad (5.3)$$

$$E_f = E_{defect}(N_4) - (E_{perfect}(NiFe_2O_4) + \mu_{Mo}) \quad (5.4)$$

In equation (5.1 - 5.4), E_f is the defect formation energy, $E_{perfect}$ represents the energy of the N0 model, E_{defect} depicts the energy of the Mo doped optimized model; μ_{Ni}, μ_{Fe}, and μ_{Mo} are the chemical potentials of Ni, Fe, and Mo atom i.e. the energy per atom. The unit cell of Ni (COD #9012985), Fe (COD #9015972), and Mo (COD #9008474) was taken from the Crystallography Open Database (COD). The geometry of the optimized model, which has the most negative defect formation energy, gives the location of the Mo dopant in the $NiFe_2O_4$ lattice.

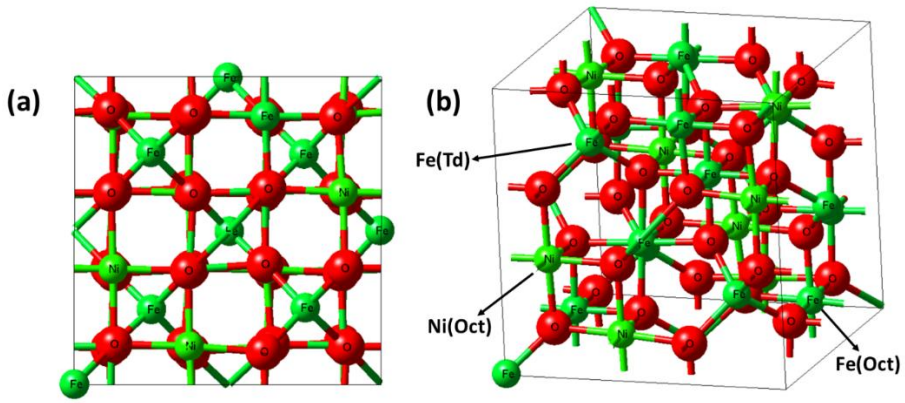

Figure 5.1. (a, and b) The optimized unit cell of $NiFe_2O_4$.

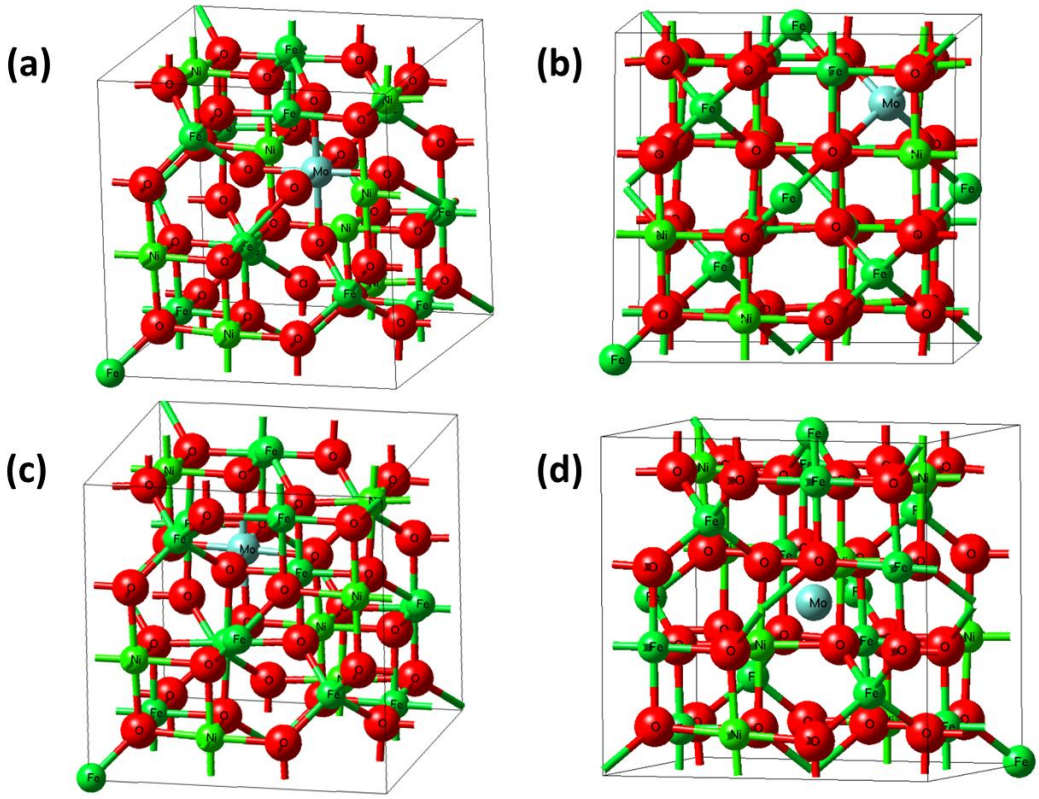

Figure 5.2 Mo-doped $NiFe_2O_4$ unit cell models. (a) Mo substituting Fe(Oct), (b) Mo substituting Fe(Td), (c) Mo substituting Ni(Oct), and (d) Mo occupying an interstitial position.

5.2.4 DFT modelling and methodology

Another set of DFT calculations was carried out to investigate the adsorption mechanism. A $NiFe_2O_4$ unit cell was taken from the materials project database (MP-22684)[204,216]. Then, a 3 x 3 x 3 supercell was built from the $NiFe_2O_4$ unit cell by the Scienomics' MAPS 4.4.1

software [82,143]. Next, a cluster of $NiFe_2O_4$ having 26 atoms was cleaved from this supercell. Hydroxyl groups were utilized to passivate the terminal (surface) atoms of the $NiFe_2O_4$ cluster using GaussView 6.0 software. The $NiFe_2O_4$ cluster has a total of 33 atoms after passivation. This cluster has three types of metal centers occupied by Ni and Fe atoms. The Ni atom has an octahedral coordination (Ni(Oct)). One type of Fe atom has an octahedral (Fe(Oct)) coordination, while the other has a tetrahedral coordination (Fe(Td)). This cluster was optimized by the DGDZVP basis set with the B3LYP (Becke-3-Parameter-Lee-Yang-Parr) functional in the Gaussian 16 software[217]. In the rest of this chapter, the optimized $NiFe_2O_4$ cluster is denoted by the NIF33.

The previously optimized Mo-doped $NiFe_2O_4$ model (section 5.2.3) with the most negative formation energy was subjected to further processing. A cluster of Mo-doped $NiFe_2O_4$ was cleaved from a suitable supercell of that model using the MAPS 4.4.1 software. The unsaturated terminal oxygens of this cluster were passivated by hydrogens in the GaussView 6.0 software. Since the cluster has been carved out of an optimized supercell, a single-point DFT calculation was performed on this cluster at the previously stated theory level. This Mo-doped $NiFe_2O_4$ cluster model is denoted by the abbreviation 'MoNIF33' cluster throughout this chapter. Natural bond orbital (NBO) analysis of NIF33 and MoNIF33 has also been investigated to understand the change in charge distribution of NIF33 after Mo doping.

CIP and MG molecules were modeled using GaussView software. These two molecules were optimized at the same level of theory as earlier. Separate calculations were run for a CIP molecule in different orientations around the NIF33 and MoNIF33 clusters. Analogous calculations were done with an MG molecule placed in different orientations around the model cluster. The interaction energies of CIP and MG with NIF33 and

MoNIF33 clusters were calculated at the same level of theory DFT calculations as earlier. All the calculations were performed in the gas phase.

5.3 Results and Discussion

5.3.1 Material characterizations

Figures 5.3a and 5.3b show the high-resolution XRD patterns of pure $NiFe_2O_4$, 1MNIF, 2MNIF, and 4MNIF nanoparticles. The XRD pattern of pure $NiFe_2O_4$ shows diffraction peaks at 18.4°, 30.2°, 35.7°, 37.3°, 43.3°, 53.8°, 57.2°, 62.9° and 74.4° (2θ) conforming to the (111), (220), (311), (222), (400), (422), (511), (440), and (533) planes of inverse spinel $NiFe_2O_4$ structure as per JCPDS File 74-2081 from the JCPDS database[218,219]. The peaks in the XRD patterns of 1MNIF, 2MNIF, and 4MNIF samples match that of $NiFe_2O_4$ (JCPDS File 74-2081). Peaks other than those belonging to pure $NiFe_2O_4$ are not present in the XRDs of the Mo-doped samples. Hence, we conclude that Mo atoms were successfully incorporated into the $NiFe_2O_4$ lattice. The Mo dopant can substitute one of the cations in the $NiFe_2O_4$ crystal structure. XPS analysis in a later section shows that Mo is present in doped $NiFe_2O_4$ only in +5 and +6 oxidation states. Table 5.1 displays the ionic radius of different metal ions present in the $NiFe_2O_4$ sample and Mo in +5 and +6 oxidation states. If Mo substitutes a bigger cation, Ni^{2+} in octahedral or Fe^{3+} in tetrahedral position, it should contract the crystal lattice. Alternatively, if Mo substitutes an octahedral Fe^{3+} (smaller cation), it should expand the lattice. Note that the XRD peaks of doped $NiFe_2O_4$ shifted slightly to lower 2θ values corresponding to higher d-spacing (interplanar distance) with increasing Mo dopant amount (Figure 5.3b). This corresponds to the expansion of the $NiFe_2O_4$ lattice parameter after Mo-doping, indicating that the dopant Mo substitutes Fe in the octahedral positions in the parent lattice. (Table 5.2 column 3). The crystallite size of each sample (in nm) was calculated using the Scherrer equation.

$$D = \frac{k\lambda}{\beta Cos\theta} \quad (5.5)$$

In equation (5.5), λ is the X-ray wavelength in nm, β is the FWHM width of the diffraction peak, θ - diffraction angle, and k- shape factor constant.

The XRD peaks of the doped sample indicate that its lattice is cubic. So, the following equation was used to calculate lattice constant 'a' in Å;

$$\frac{1}{d_{hkl}} = \frac{\sqrt{h^2+k^2+l^2}}{a} \quad (5.6)$$

In equation (5.6), d_{hkl} is the interplanar distance (nm) at (h,k,l) miller index of the diffracted plane.

Table 5.1 The ionic radii of the cations in the undoped $NiFe_2O_4$ and Mo-doped $NiFe_2O_4$. Note- Oh and Td represents octahedral and tetrahedral coordination, respectively.[220]

Metal ion	**Ionic radii (Å)**
Ni^{2+}(oh)	0.69
Fe^{3+}(Td)	0.49
Fe^{3+}(oh)	0.55
Mo^{5+}(oh)	0.61
Mo^{5+}(Td)	0.46
Mo^{6+}(oh)	0.59
Mo^{6+}(Td)	0.41

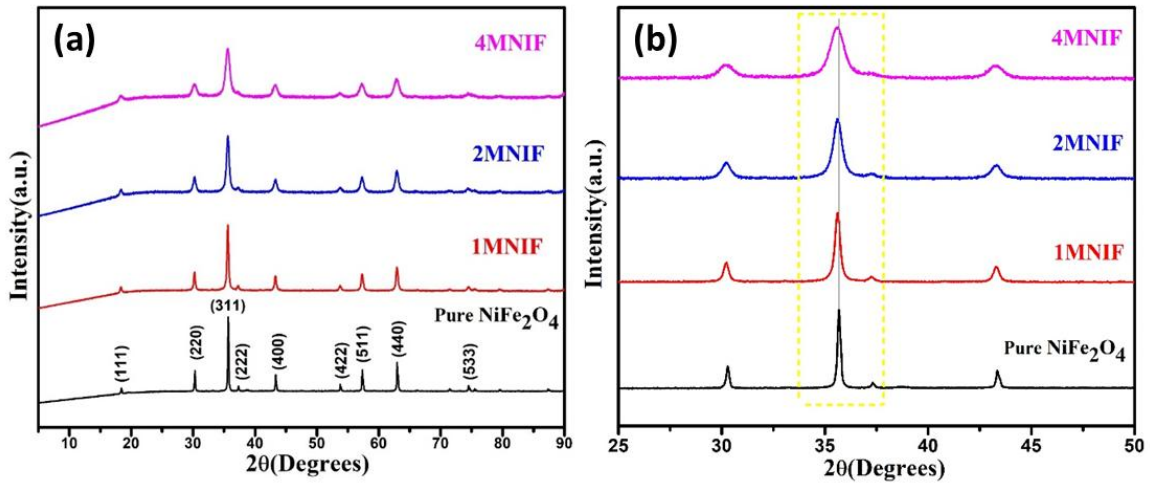

Figure 5.3 (a) XRD of pure $NiFe_2O_4$, 1MNIF, 2MNIF, and 4MNIF samples. Part (b) of the figure displays the 25° to 50° (2θ) region only to illustrate the shift in peaks with Mo-doping.

Table 5.2 Structural parameters for $NiFe_2O_4$, 1MNIF, 2MNIF, and 4MNIF nanoparticles. Equations 5.5 and 5.6 were used to calculate these structural parameters.

Nanoparticle sample	Crystallite size (nm)	Lattice parameter (Å)
Pure $NiFe_2O_4$	42.87	8.343
1MNIF	27.02	8.344
2MNIF	17.34	8.347
4MNIF	28.05	8.358

Column 2 of Table 5.2 displays the crystallite size of the doped and undoped $NiFe_2O_4$ samples. The crystallite size of $NiFe_2O_4$ decreased from 42.87 to 17.34 nm as the Mo-dopant percentage was increased to two (2MNIF). The increase in crystallite size after 2MNIF could be because Mo doping beyond a certain limit into the $NiFe_2O_4$ lattice restricts the crystallite growth by slowing the rate of nucleation during sample crystallization[221], increasing the crystallite size in the last entry of Table 5.2.

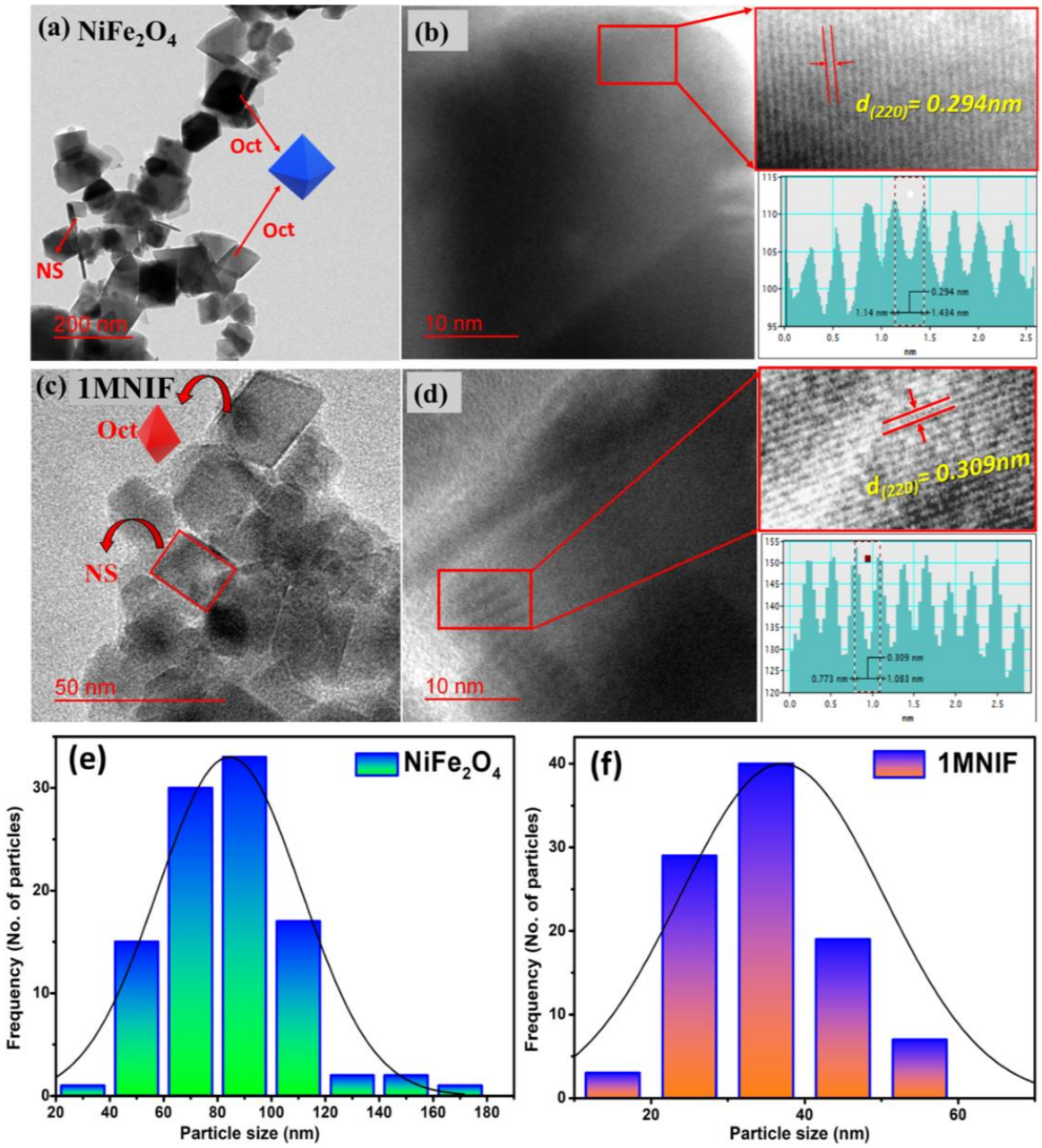

Figure 5.4 (a)TEM and (b) HR-TEM images of $NiFe_2O_4$ nanoparticles. (c) TEM and (d) HR-TEM images of the 1MNIF nanoparticles. Particle size distribution plots of (e) $NiFe_2O_4$, and (f) 1MNIF samples. (Note- NS denotes nano-sheet, Oct denotes octahedron.)

Figure 5.4a shows that the particles of pure $NiFe_2O_4$ have octahedral and nano-sheet-like shapes. The calculated lattice d-spacing of 0.294 nm from the HR-TEM image of pure $NiFe_2O_4$ (Figure 5.4b) matches with the FCC $NiFe_2O_4$ (111) lattice plane (JCPDS no.-74-2081). The d-spacing between two adjacent lattice planes were measured by ImageJ

software. The discussion in the forthcoming section 5.3.2 shows that 1MNIF has the best adsorption capacity among the Mo-doped $NiFe_2O_4$ samples investigated in this study. Hence, most material characterizations are restricted to pure $NiFe_2O_4$ and 1MNIF samples. Figure 5.4c shows the morphology of 1MNIF particles. The shape of 1MNIF particles remain approximately octahedral even after Mo-doping. The HR-TEM image of 1MNIF (inset in figure 5.4d) displays lattice fringes with spacing of 0.31 nm, in agreement with the (220) lattice plane. This increase in d-spacing conforms with the XRD observations and demonstrates successful doping of molybdenum into the $NiFe_2O_4$ nanoparticles. Figure 5.4e and 5.4f show the particle size distribution of $NiFe_2O_4$ and 1MNIF samples using ImageJ software. Mo doping of $NiFe_2O_4$ decreases the average particle size from 80-90 nm ($NiFe_2O_4$) to 30-40 nm (1MNIF). The Polydispersity index (PDI) of $NiFe_2O_4$, and 1MNIF samples was also calculated by using TEM data. Equations 5.7 and 5.8 were used to calculate the polydispersity index (PDI).

$$PDI = \left(\frac{\sigma}{D_{avg}}\right)^2 \qquad (5.7)$$

In Eq. 5.7, σ represents the standard deviation of particle size distribution, D_{avg} denotes the average particle size of a sample. Equation 5.8 was used to calculate the standard deviation (σ) using particle size distribution data.

$$\sigma = \sqrt{\frac{\sum(D_i - D_{avg})^2}{N}} \qquad (5.8)$$

In eq. 5.8, D_i denotes size of each particle, and N is the total number of particles.

Before Mo doping, pristine $NiFe_2O_4$ exhibited a PDI of 0.099**,** indicating a monodisperse nanoparticle distribution. In contrast, the 1MNIF sample displayed a PDI of 0.126**,** suggesting a transition to a moderately polydisperse nanoparticle system.

Figure 5.5a and 5.5b shows a SEM micrograph of the as synthesized 1MNIF nanoparticles and its elemental mapping. The latter shows that the Mo-dopant is homogeneously distributed in the 1MNIF sample (Figure 5.5b).

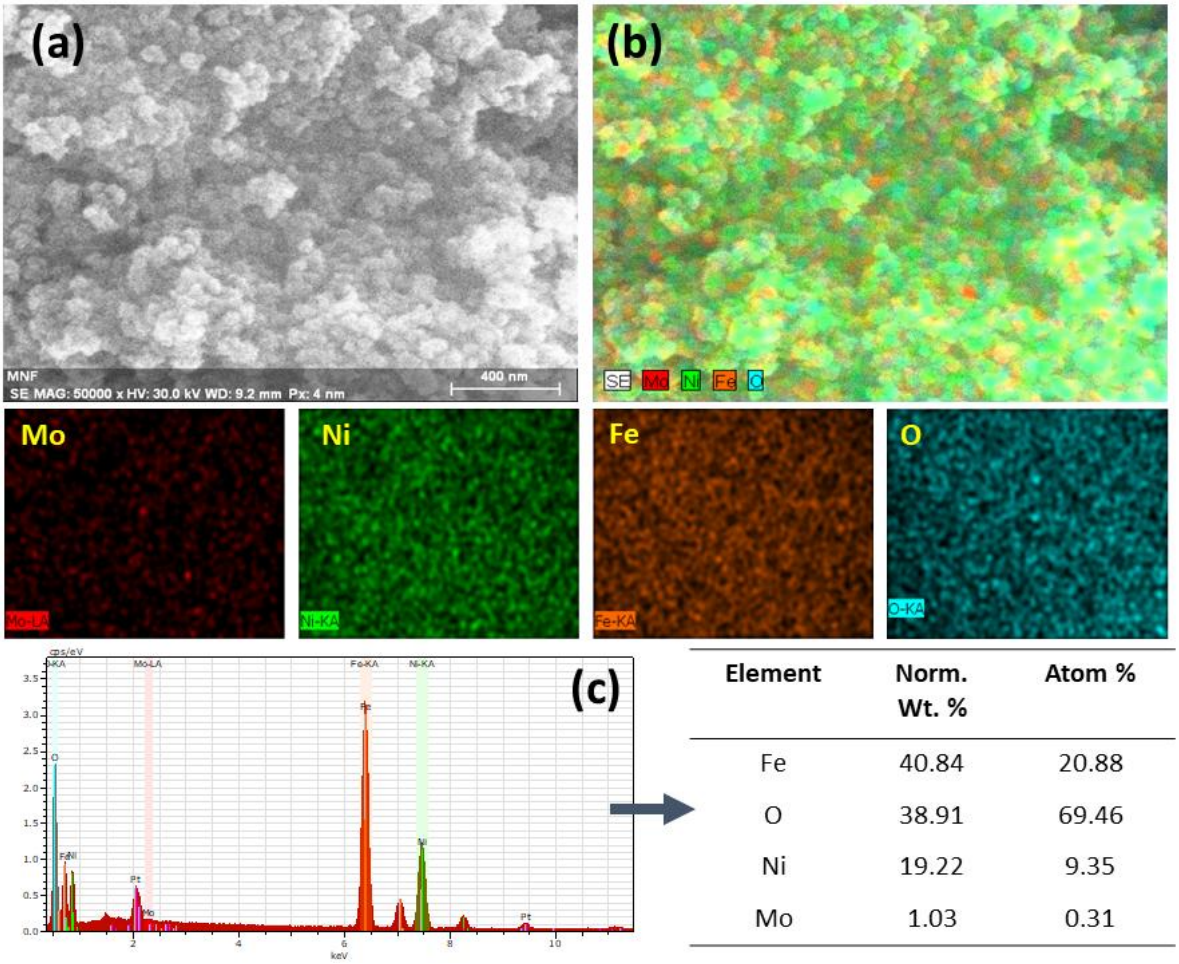

Element	Norm. Wt. %	Atom %
Fe	40.84	20.88
O	38.91	69.46
Ni	19.22	9.35
Mo	1.03	0.31

Figure 5.5 (a) SEM images, (b) elemental mapping, and (c) EDX analysis with atomic percent of elements in the 1MNIF sample.

The pH level at which there is no net charge on the adsorbent's surface is known as the point of zero charge (pH_{pzc}). At $pH<pH_{pzc}$, the adsorbent's net charge will be positive; at $pH > pH_{pzc}$, the net charge will be negative. Zero-point charge analysis gives the idea of adsorbate-adsorbent interaction due to surface electrostatic charge. This analysis was done by the salt addition method. Figure 5.6a displays the pH_{pzc} of 1MNIF is at 7.6 pH.

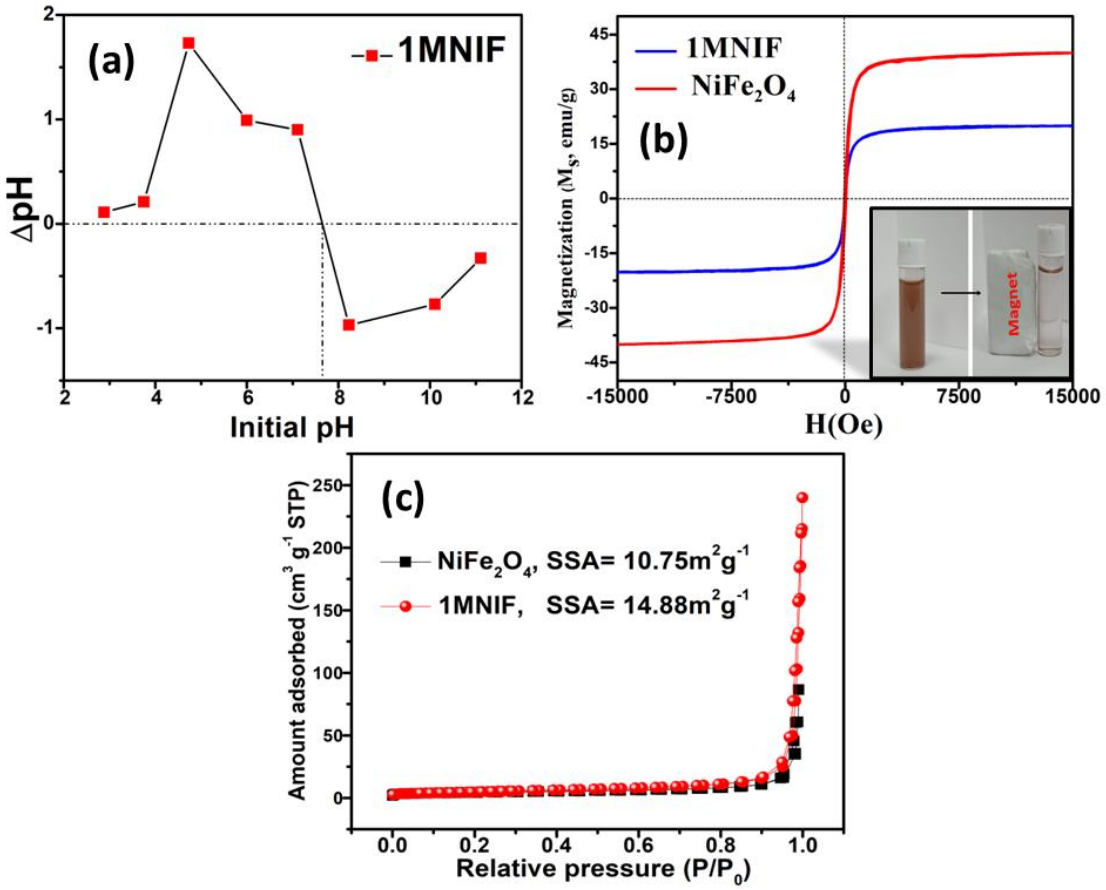

Figure 5.6 (a) Plot between ΔpH and initial pH to determine the point of zero charge (pH_{pzc}) of 1MNIF, (b) Magnetization versus applied magnetic field plots for $NiFe_2O_4$ and 1MNIF samples, and (c) BET plots of pure $NiFe_2O_4$, and 1MNIF nanoparticles. (SSA denotes specific surface area.)

Figure 5.6b shows the magnetization (emu/g) against the applied magnetic field (O_e) plots using Vibrating sample magnetometer (VSM) for pure $NiFe_2O_4$ and 1MNIF samples. The saturation magnetization for pure $NiFe_2O_4$ is 39.7 emu/g. Mo-doping decreased the saturation magnetization of 1MNIF to 20.2 emu/g. The absence of a hysteresis loop indicates that the pure and doped samples are superparamagnetic. The inset image shows that the saturation magnetization values are sufficient for the magnetic separation of these particles from water by a suitable magnet.

The surface area of the adsorbent plays a crucial role in its performance. The surface area of pure $NiFe_2O_4$ and 1MNIF nanoparticles was determined using the BET N_2 adsorption-desorption isotherm technique. Figure 5.6c shows the BET graph plotted between the amount adsorbed ($cm^3\ g^{-1}$ STP) versus relative pressure (P/P_0). The BET plots for both samples belong to the type-III isotherm class. Pure $NiFe_2O_4$ has a BET-specific surface area of 10.75 $m^2\ g^{-1}$. Mo-doping increased the surface area of the 1MNIF adsorbent to 14.88 m^2g^{-1}. On the other side, the average pore diameters of pure $NiFe_2O_4$ and 1MNIF samples are 38.83 and 84.67 nm, indicating the meso and macroporous nature of the adsorbent, respectively.

The XPS of pure $NiFe_2O_4$ and 1MNFO samples were carried out to determine the chemical composition of the photocatalyst surface and the oxidation states of the elements present. Figure 5.7a displays the Ni2p spectrum of $NiFe_2O_4$ and 1MNFO samples. The $NiFe_2O_4$ spectrum has Ni2$p_{3/2}$, and Ni2$p_{1/2}$ spin orbit doublets at 854.97 eV and 872.58 eV binding energies (B.E.) with two shake-up satellite peaks (denoted as 'sat.' in Figure 5.7a), indicating Ni^{2+} occupies octahedral sites.[219] The fitted Ni 2p core-level spectrum of 1MNFO (Fig. 5.7a) also exhibits two shake-up satellites and spin-orbit doublets (Ni 2$p_{3/2,}$ Ni 2$p_{1/2}$). The Ni 2$p_{3/2}$ and Ni 2$p_{1/2}$ spin-orbit doublets at 855.39 and 873.02 eV show that Ni^{2+} occupies octahedral sites in the 1MNFO crystal structure.[219]

Figure 5.7b compares the Fe2p regions of bare $NiFe_2O_4$ and 1MNFO samples. The Fe2p spectrum has two spin-orbit doublets (Fe 2$p_{3/2,}$ Fe 2$p_{1/2}$) and two satellite peaks (denoted as 'Sat.' in Figure 5.7b). Further deconvolution gave peaks at 709.98, 712.14, and 723.65, 726.28 eV, with two satellite peaks at 718.46 and 732.66 eV. These show that Fe^{3+} occupies octahedral and tetrahedral sites of the $NiFe_2O_4$ lattice.[196,222–224] The Fe 2p spectrum of 1MNFO also displays the Fe 2$p_{3/2}$ and Fe 2$p_{1/2}$ spin-orbit doublets. The Fe2$p_{3/2}$

part is deconvoluted into 710.10 and 712.30 eV, while the Fe2$p_{1/2}$ part fits peaks at 723.69 and 726.59 eV. These peaks, in combination with two satellite peaks at 718.59 and 732.51eV binding energies, show that Fe^{3+} occupies octahedral and tetrahedral sites of the 1MNFO sample.[196,224] A comparison of the spectrum of $NiFe_2O_4$ and 1MNFO reveals that Mo-doping shifts the deconvoluted Fe2p peaks to slightly higher binding energies.

Figure 5.7c presents the O1s spectra of pure $NiFe_2O_4$ and 1MNFO samples. For pure $NiFe_2O_4$, three distinct deconvoluted peaks are observed at binding energies of 529.73, 531.0, and 532.18 eV, corresponding to metal-oxygen bonds (Ni-O or Fe-O)[192,225], oxygen vacancies[226,227], and chemisorbed oxygen in -OH groups[227,228], respectively (Figure 5.7c). Upon Mo doping, the lattice oxygen deconvoluted O1s peak shifts to a slightly lower 529.71eV binding energy[192,225]. The other two O1s peaks shift to slightly higher 531.27 and 532.34 eV binding energies. These are also attributed to oxygen vacancies[226,227] and chemisorbed oxygen[227,228] species, respectively (Figure 5.7c). However, the area of oxygen vacancy peak and chemisorbed oxygen peak of pure $NiFe_2O_4$ decreased after Mo doping. This indicates that Mo dopants utilized chemisorbed oxygen to compensate for the oxygen vacancy and maintain charge balance in the lattice.

Figure 5.7d displays the Mo 3d fitted spectrum region. Two major peaks are observed at 232.25 (Mo 3$d_{5/2}$) and 235.18 eV (Mo 3$d_{3/2}$) binding energies. Each of these peaks could be deconvoluted into two more peaks. The peaks at 231.78 and 235.06 eV indicate the presence of Mo in the +5-oxidation state, while the peaks at 232.35 and 235.76 eV correspond to Mo in the +6 state[229–232]. The higher valent Mo (in +6 oxidation state) dopant substitutes a Fe site in the $NiFe_2O_4$ lattice, causing oxygen deficiency. Oxygen vacancies are electron-rich, enabling the reduction of the higher-valent Mo^{6+} ions to Mo^{5+} ions[213,231,232]. Since higher-valent dopants require additional oxygen to maintain charge

balance within the lattice, they tend to utilize chemisorbed oxygen to compensate for the oxygen deficiency. Consequently, this process leads to a reduction in the overall percentage of oxygen vacancies in the lattice. Overall, Mo doping causes a slight shift in the Ni 2p and Fe 2p peaks towards higher binding energies. Concurrently, the lattice oxygen peak shifts to lower binding energy. These observations suggest that Mo doping facilitates charge transfer from the Ni and Fe sites to the lattice oxygen.

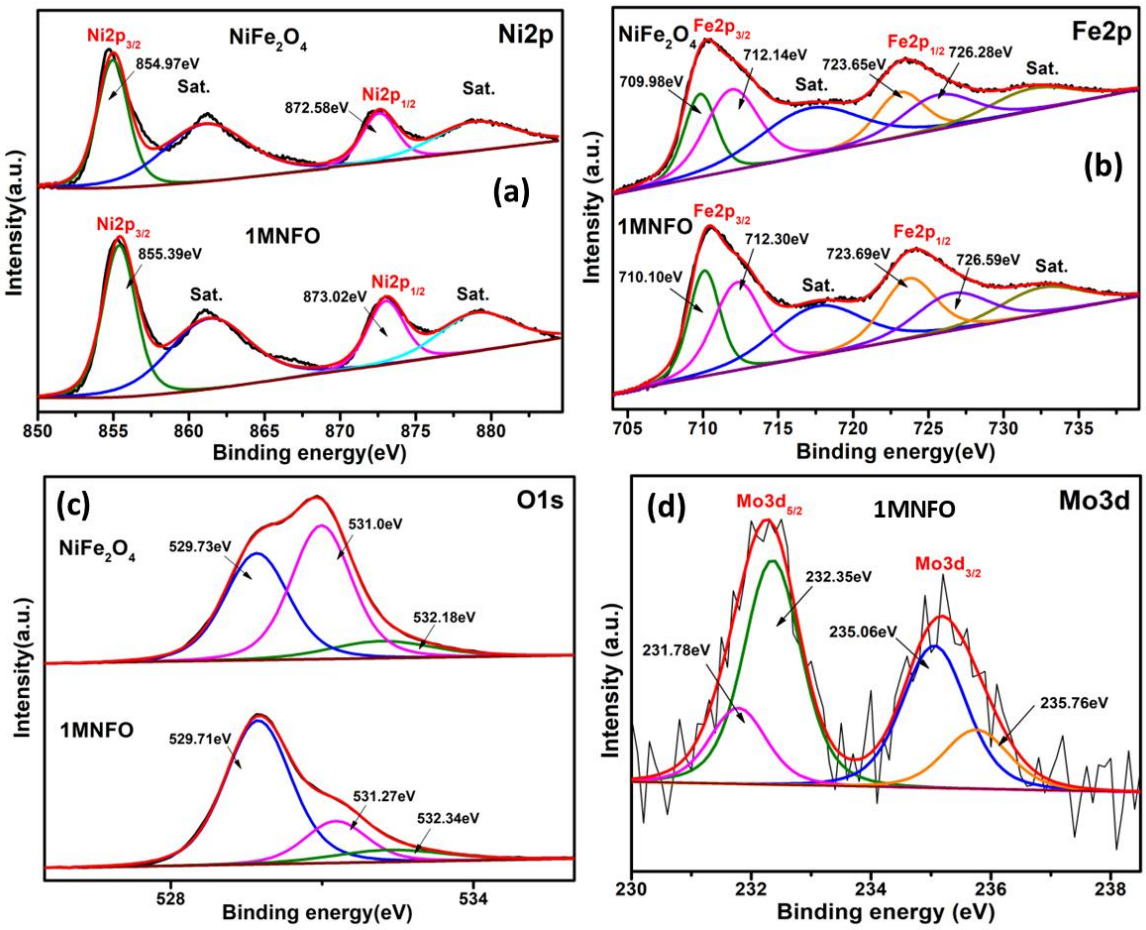

Figure 5.7 High resolution comparative XPS spectra of, (a) Ni2p, (b) Fe2p, (c) O1s, and (d) Mo3d in pure $NiFe_2O_4$ and 1MNIF samples.

5.3.2 Adsorption studies

Adsorption studies were conducted to examine the impact of the adsorbent dosage on the co-adsorption of MG and CIP, with the different amounts (0.01 to 0.04 g) of adsorbent in

20 ml of mixed solution of CIP and MG. The adsorption capacity of the adsorbent increases with a decrease in the adsorbent amount (Fig. 5.8a). Hence, the optimum adsorbent dose was 0.010 g for all subsequent adsorption experiments.

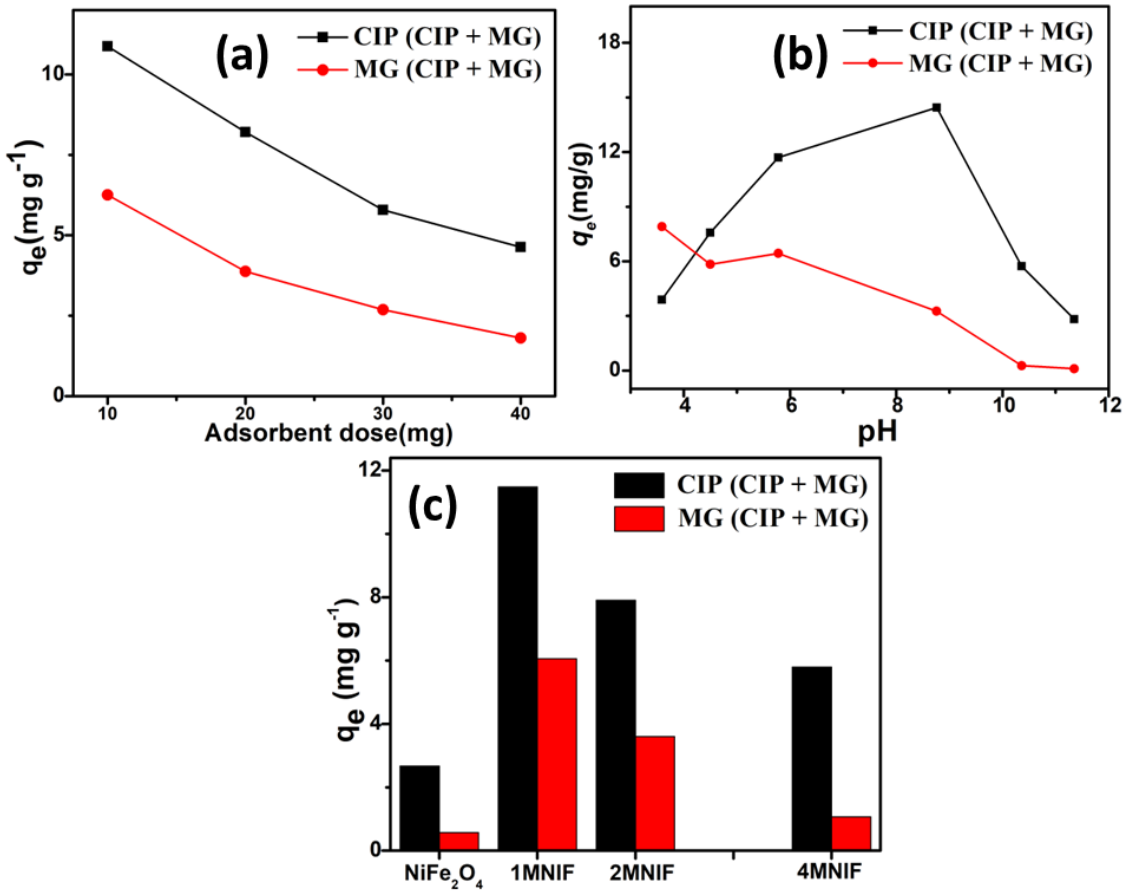

Figure 5.8 (a) Effect of amount of adsorbent (1MNIF) on the co-adsorption of CIP and MG. (b) Effect of pH on the co-adsorption of CIP and MG, and (c) Effect of Mo dopant percentage in $NiFe_2O_4$ on the adsorption of MG and CIP from the binary (CIP + MG) solution. (Conditions- The binary solution of MG and CIP was synthesized by mixing equal volumes of each 6 mg L^{-1} MG and 18 mg L^{-1} CIP solution. All experiments were done with 20ml of the adsorbate solution, 300K temperature, and 24-hour time.)

The equilibrium CIP and MG adsorption capacities of 1MNIF (from the binary adsorbate system) were investigated at different pH values. These experiments were conducted on binary solutions containing equal volumes of 18 mg L^{-1} CIP and 6 mg L^{-1} MG aqueous solutions. Figure 5.8 (b) shows the change in the adsorption capacity of CIP

and MG on 1MNIF with pH. The CIP adsorption capacity reaches its peak around pH 8.5. The 1MNIF adsorbent has a point of zero charge (PZC) of approximately 7.6, and therefore the adsorbent has positive surface charges at pH < 7.6 and negative surface charges at pH > 7.6. CIP molecules are generally in zwitterionic state[38,233] in the solution for pH 7 to 8.5, and 1MNIF adsorb these molecules as a result of electrostatic interactions. On increasing the solution pH below 8.5, adsorption capacity for CIP decreased due to electrostatic repulsion between negative charged 1MNIF adsorbent and CIP anion. The 1MNIF exhibited higher adsorption capacity for MG dye in slightly acidic and neutral pH. Since pKa of MG dye is 3.6, at pH = 6 it is predominantly anionic in nature. At pH 6 the 1MNIF adsorbent surface has a positively surface charge potential which attracts the anionic dye. Overall, it was decided that the optimum solution pH for co-adsorption of these two solutes from their binary (CIP+MG) solution is 6. Hence, all subsequent adsorption experiments on the 1MNIF sample were carried out at this pH.

Figure 5.8c shows the effect of Mo dopant percentage in $NiFe_2O_4$ adsorbent on its equilibrium adsorption capacity for CIP and MG from their binary solution. The CIP and MG adsorption capacity of 1MNIF is maximum among different adsorbents prepared in this study. The adsorption capacity decreases with increase in Mo-dopant percentage in $NiFe_2O_4$. Given this preliminary observation, subsequent detailed adsorption isotherm experiments were performed only with the 1MNIF adsorbent.

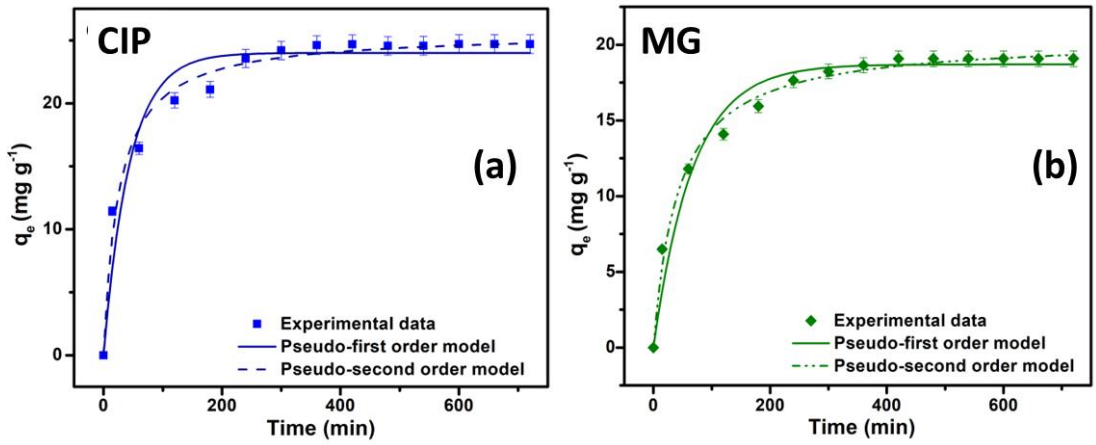

Figure 5.9 Adsorption kinetics for (a) CIP and (b) MG from their aqueous solutions. (Reaction condition- Pollutant- separate CIP (48 mg L^{-1}) and MG (16 mg L^{-1}) solution for single adsorbate system, Adsorbent dose- 0.010 g, pH-neutral, 300K temperature, and 24-hour time.)

Adsorption kinetics is critical for understanding adsorption rates, and mass transfer mechanisms. The kinetics of adsorption of MG and CIP from their individual aqueous solutions was first investigated. Figures 5.9 shows the adsorption capacity ('q_t', mg/g) of adsorbent (1MNIF) versus time ('t', minute) for adsorption of MG and CIP from single adsorbate systems. The adsorption capacities of 1MNIF for adsorption of MG and CIP from their individual aqueous solutions reached saturation or near saturation within 300 min. The adsorption kinetics data of MG and CIP on the 1MNIF adsorbent were fitted to pseudo-first-order (PFO) and pseudo-second order (PSO) adsorption kinetics models.

Table 5.3 Various kinetics parameters obtained from the nonlinear fitting of pseudo first and pseudo second order kinetics model.

System	Adsorbate	Pseudo-first-order kinetics			Pseudo-second-order kinetics		
		k_1(min^{-1})	q_e (mg.g^{-1})	R^2	k_2(g.mg^{-1}.min^{-1})	q_e(mg.g^{-1})	R^2
Single	CIP	0.023	24.002	0.950	0.003	25.628	0.994
	MG	0.015	18.703	0.966	0.002	20.459	0.992

Table 5.3 includes various kinetics parameters obtained from the nonlinear fitting of pseudo-first and pseudo-second-order kinetics models for the adsorption of CIP and MG by 1MNIF adsorbent. In all cases, the non-linear fitting correlation coefficient (R^2) was substantially higher for the pseudo-second-order kinetic model. Hence, the adsorption of CIP and MG individually on the 1MNIF adsorbent follow pseudo-second-order-kinetics. Nevertheless, extending this inference for adsorption from a binary solution may not be correct. Note that to the best of our knowledge there is no binary adsorption kinetics model in literature. Hence, no attempt has been made to investigate the binary adsorption kinetics of this co-adsorption research problem.

Isothermal equilibrium adsorption data are crucial for comprehending the mechanism underlying the adsorption process. Adsorption isotherms are plots of adsorption capacity (mg g^{-1}) versus adsorbate (mg L^{-1}) concentration remaining in the solution. Extended adsorption isotherm models were used to analyze co-adsorption from binary solutions (CIP+MG). The Extended Langmuir (EL), Extended Freundlich (EF) and Extended Langmuir-Freundlich (ELF) isotherms was utilized for nonlinear adsorption isotherm fitting [201,234].

Table 5.4 Extended adsorption isotherm parameters obtained for the non-linear fitting of CIP and MG adsorption from their binary solution.

Adsorbate in binary system	**Extended Freundlich isotherm parameters**					
	x_i	y_i	z_i	k_i (L.mg^{-1})	n_i	R^2
CIP (CIP+MG)	74.55	1.17	7.74	0.63	1.10	0.989
MG (CIP+MG)	18.67	3.80	6.68	5.44	1.48	0.991
Adsorbate in binary system	**Extended Langmuir isotherm parameters**					
	q_{m1} (mg.g^{-1})		q_{m2} (mg.g^{-1})	b_1 (L.mg^{-1})	b_2 (L.mg^{-1})	R^2
CIP (CIP+MG)	24.70		---	0.11	---	0.78
MG (CIP+MG)	---		19.90	---	0.16	0.81
Adsorbate in binary system	**Extended LF isotherm parameters**						
	q_{m1} (mg.g^{-1})	q_{m2} (mg.g^{-1})	b_1 (L.mg^{-1})	b_2 (L.mg^{-1})	n_1	n_2	R^2
CIP (CIP+MG)	22.70	---	5.45	---	1.45	---	0.92
MG (CIP+MG)	---	18.95	---	5.04	---	9.24	0.86

Table 5.4 gives the parameters for the fitting of experimental adsorption isotherm data of CIP and MG (from their binary solutions) to the EL, EF and ELF adsorption isotherm models. The equilibrium adsorption data for CIP and MG from their binary solution fits best the EF isotherm ($0.98<R^2<0.99$) model (Figure 5.10). Fits of this data to the EL and ELF isotherms are poor. A best fit to the EF isotherm shows that the adsorbent uses heterogeneous sites for adsorbing MG and CIP.

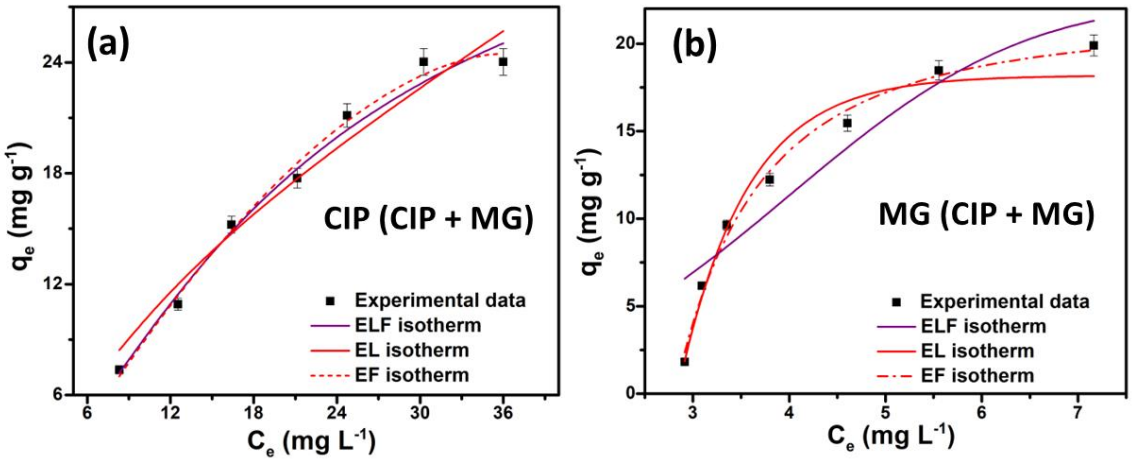

Figure 5.10 (a, and b). Nonlinear adsorption isotherms for CIP and MG adsorbates in binary adsorbate system. (Reaction condition- adsorbate- 20 ml of mixture of each CIP (12-48 mg L^{-1}) and MG (4-16 mg L^{-1}) solution for binary adsorbate system, Adsorbent dose- 0.010 g, pH-neutral, 300K temperature, and 24-hour time.)

The FTIR spectra of 1MNIF adsorbent after CIP and MG adsorption were recorded and compared with unused 1MNIF sample. Figure 5.11 compares the FTIR spectra of the unused 1MNIF adsorbent and 1MNIF after adsorption of MG and CIP from their single and binary adsorbate solution. Table 5.5 (a and b) shows the assignment of functional group present in the sample for specific peaks present in the FTIR spectrum. The CIP molecule adsorbed to the surface of 1MNIF through its -F, -COOH functional group in the CIP+1MNIF. The MG molecule adsorbed through its azo and $-SO_3H$ functional group in MG+1MNIF sample. In binary adsorbate system, the peaks assigned to the above-

mentioned functional groups of CIP and MG, show slight shifting. This could be due to external repulsion or attraction from another adsorbate also adsorbed on the 1MNIF surface.

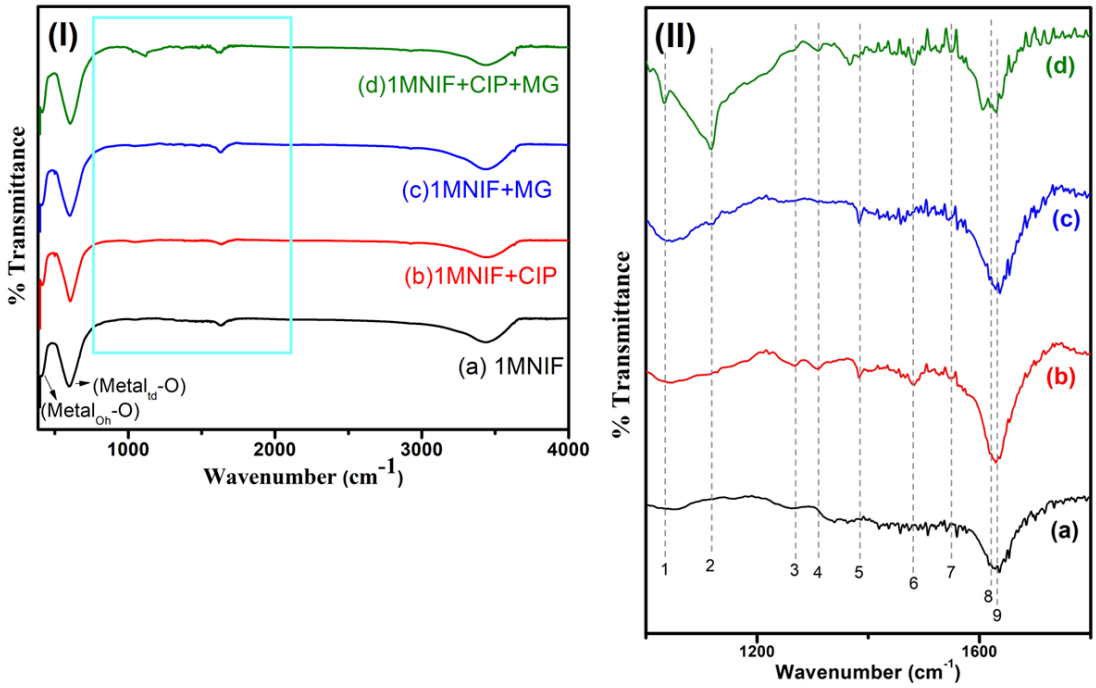

Figure 5.11 (I and II). FTIR spectra of (a) unused 1MNIF sample, (b) CIP adsorbed 1MNIF sample (CIP+1MNIF), (c) MG adsorbed 1MNIF sample (MG+1MNIF), and (d) CIP, MG adsorbed 1MNIF sample (CIP+MG+1MNIF). (Note that $Metal_{Oh}$ means metal present in octahedral void, and $Metal_{Td}$ means metal present in tetrahedral voids in the 1MNIF lattice.)

Table 5.5a FTIR peak assignment for different samples.

CIP+1MNIF	MG+1MNIF	CIP+MG+1MNIF	Functional group present
1045.6		1033.7	C-F stretching
	1118.7	1115.1	S=O stretching
1267.1		1265.5	C-N aromatic amine
1309.5		1310.5	O-H bending

1385.5	1383.6	1368.8	C-N stretching
1480.6		1484.8	Aromatic C-O stretching
1549.0	1548.7	1564.4	Cyclic C=C vibration
1630.7		1619.22	Quinolinic N-H bending
	1638.2	1629.4	-N=N bond stretching

Table 5.5b FTIR peaks assignment for common peaks present in different samples.

CIP+1MNIF	MG+1MNIF	CIP+MG+1MNIF	Functional group present
2922.4	2921.4	2923.5	Cyclopropyl C-H, asymmetric -CH_3 stretching
3438.7	3459.7	3441.9	O-H stretching
3633.7	3633.9	3637.2	N-H stretching

Figure 5.11(I) shows the FTIR spectra of unused 1MNIF, CIP adsorbed 1MNIF (CIP+1MNIF), MG adsorbed 1MNIF (MG+1MNIF), and CIP, MG adsorbed 1MNIF sample from their binary (CIP+MG) solution. Figure 5.11 (II) compares the FTIR spectra of the unused 1MNIF adsorbent and 1MNIF after adsorption of CIP and MG from the single and binary solution in the fingerprint region. Table 5.5a presents the peak position assigned to specific functional group from the literature survey[235–238]. In the FTIR of unused 1MNIF sample, two peaks at 414.5 and 598.1 cm^{-1}, correspond to $Metal_{Oh}$-O, and $Metal_{Td}$-O bond vibrations, respectively. (Note that Metal can be Ni, Fe, or Mo present in 1MNIF adsorbent) The comparison plots show that there is a blue shift and broadening in the peaks assigned to the metal-oxygen bonds (400-850 cm^{-1}) after CIP and MG adsorption due to formation of new bond with metal present in 1MNIF adsorbent. Table 5.5a depicts the new peaks in the FTIR spectrum of CIP+1MNIF, MG+1MNIF, and CIP+MG+1MNIF due to adsorption

of CIP and MG. In the FTIR spectrum of CIP+1MNIF, the peaks at 1045.6, 1309.5, 1480.6, and 1630.7cm^{-1} were assigned to C-F stretching vibration, O-H bending vibration, C-O stretching vibration of COOH group, and quinolinic N-H bending vibration of CIP molecule. A slight shifting in these peaks were observed in FTIR spectrum of CIP+MG+1MNIF system. In the FTIR spectrum of MG+1MNIF, the peaks were observed at 1118.7, and 1638.2 cm^{-1} corresponds to -S=O stretching vibrations of $-SO_3H$, and -N=N stretching vibration of azo functional group of adsorbed MG molecule. These peaks show blue shift in the FTIR spectrum of the CIP+MG+1MNIF system. The adsorption of MG occurs on the 1MNIF surface through its -N=N, and $-SO_3H$ group in both single and binary adsorbate systems. This peak shifting may happen because in binary adsorbate system, one adsorbate may experience attraction or repulsion from another type of (neighbourhood) adsorbate. Some of the peaks at ~2920 (for cyclopropyl C-H and asymmetric $-CH_3$ stretching), ~3400-3460 (O-H stretching), and ~3635 (N-H stretching) cm^{-1} were common in the FTIR spectrum of CIP+1MNIF, MG+1MNIF, and CIP+MG+1MNIF due to presence of same functional groups (Table 5.5b). Some other unknown peaks appear in the FTIR spectrum of 1MNIF+CIP+MG, due to intermolecular interaction between the CIP and MG adsorbates after they adsorbed on the 1MNIF surface.

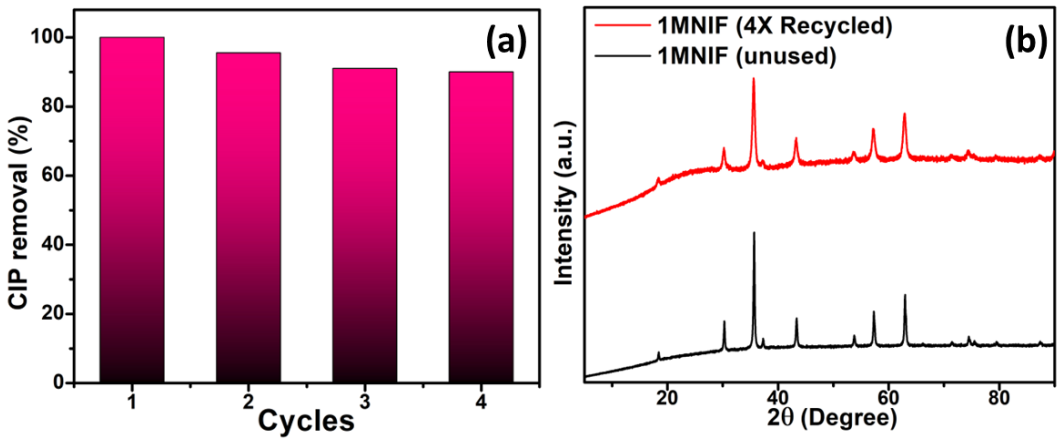

Figure 5.12 (a) Recyclability test of 1MNIF adsorbent, and (b) XRD analysis of unused and recycled 1MNIF adsorbent.

To be economically viable, the adsorbent should be recyclable with little decrease in its adsorption capacity. Four cycles of adsorption were performed to check the recyclability of the as-synthesized 1MNIF adsorbent. The corresponding CIP removal efficiency of the adsorbent from the binary solution (of MG and CIP) is plotted in the histogram format in Figure 5.12a . The figure shows that after four cycles, there is a slight reduction in the CIP removal ability of the adsorbent. Figure 5.12b compares the XRD of the recycled sample with fresh 1MNIF sample. The XRD of the reused sample shows all the peaks observed in the fresh 1MNIF sample. Moreover, the XRD of the reused 1MNIF sample shows no peaks other than those attributed to $NiFe_2O_4$.

5.3.3 DFT calculation results

DFT calculations give additional evidence supporting the experimental findings. The plane wave DFT calculations were performed to find the location of Mo dopant in $NiFe_2O_4$ lattice. The defect formation energies of N1, N2, N3, and N4 models were -0.32 eV, 0.52eV, -0.08 eV, and 27.41eV. Thus, the model (N1), in which Mo substitutes Fe(Oct) atom, is most stable. Table 5.6 shows the expansion in $NiFe_2O_4$ lattice in all three dimensions after Mo doping. Notably, the XRD data analysis corroborates the DFT findings, confirming that Mo preferentially substitutes the Fe at the octahedral site. As detailed in section 5.2.3, all subsequent DFT calculations were carried out on a Mo-doped $NiFe_2O_4$ cluster carved out of N1 called the 'MoNIF33' model. In this cluster (having total 33 atoms), Ni occupies an octahedral site (abbreviated as Ni(Oct)), Mo occupies another octahedral site (denoted as Mo(Oct)), one Fe occupies an octahedral site (abbreviated as Fe(Oct)) and another Fe is in a tetrahedral site (denoted by Fe(Td)). Figure 5.13(a-d) shows the optimized structure of NIF33, MoNIF33 cluster, CIP, and MG molecules.

Table 5.6 The change in lattice parameter for Mo substituted Fe(Oct) in $NiFe_2O_4$ lattice.

Lattice parameter	Pure $NiFe_2O_4$ (Å)	Mo doped $NiFe_2O_4$ (N1 model) (Å)
A	8.254	8.280
B	8.262	8.303
C	8.303	8.340

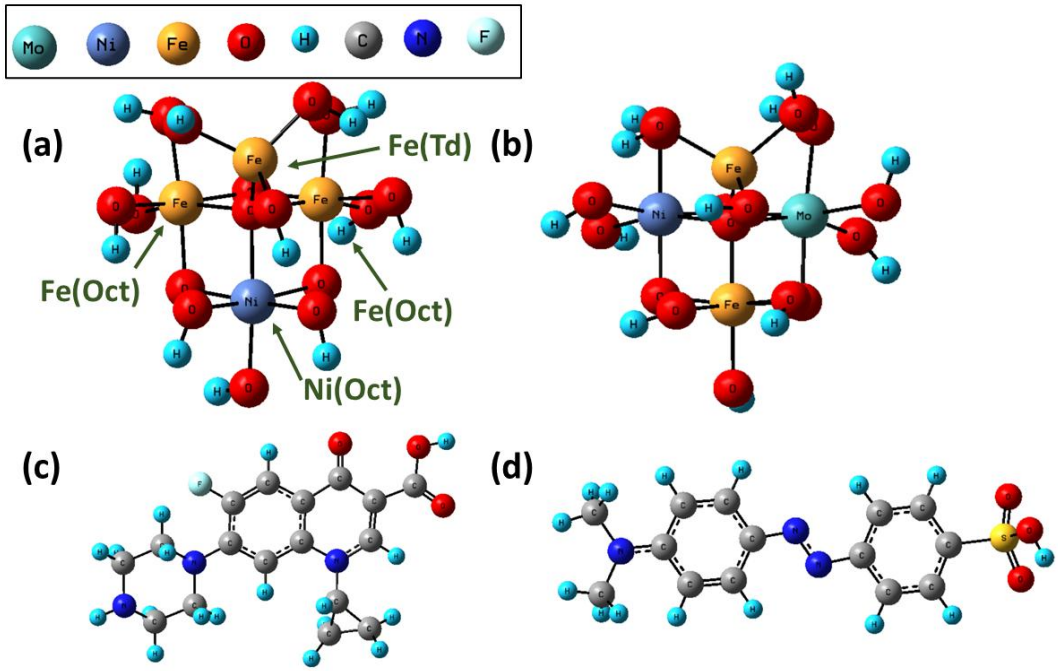

Figure 5.13 The optimized structure of (a) NIF33 cluster, (b) MoNIF33 cluster, (c) CIP, and (d) MG molecule.

Single point NBO calculations were carried out at the same theoretical level on optimised models of NIF33 and MoNIF33 (Table 5.7). Through NBO analysis, the second-order stabilization energy, also known as delocalization energy $E^{(2)}$, is determined by electron delocalization with respect to the corresponding natural Lewis structure[239,240]. The $E^{(2)}$ values give a quantification of the delocalization modifications to the natural Lewis structure [239,241] This value is calculated by Equation (5.9) employing second-order perturbation theory this calculation[240].

$$E^{(2)} = q_i \frac{(F_{i,j})^2}{(\varepsilon_j - \varepsilon_i)}, \qquad (5.9)$$

In equation (5.9), q_i = donor orbital occupancy, ε_i = energy of accepter NBO, ε_j = energy of donar NBO, $F_{i,j}$ =off diagonal Fock matrix element.

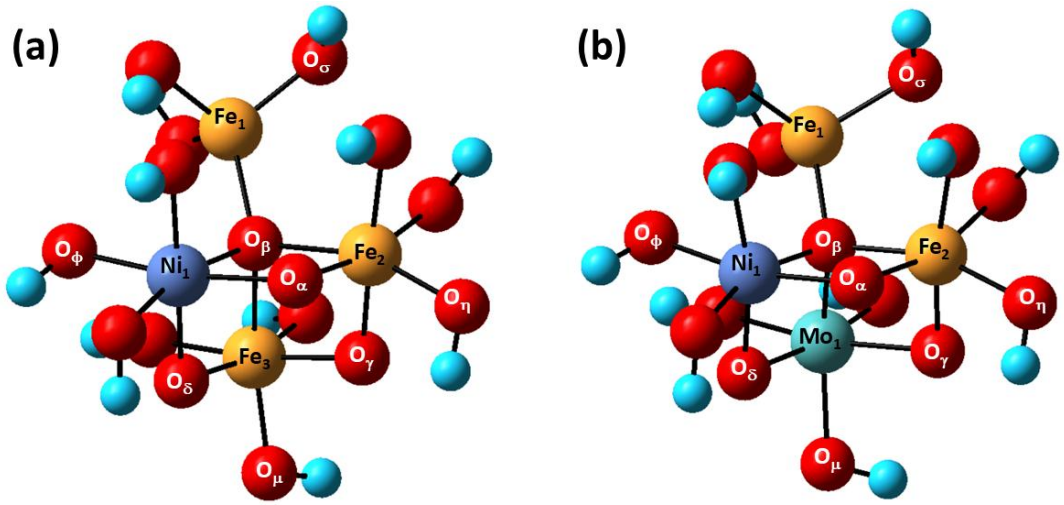

Figure 5.14 The labelling of atoms present in (a) NIF33, and (b) MoNIF33 systems, used for NBO analysis.

Table 5.7 The delocalization energy ($E^{(2)}$ in kcal/mol) calculated for charge transfer from donor to acceptor NBO of the NIF33 and MoNIF33 systems. In the table, "LP" represents the 1-center nonbonding lone pair electrons, "LP*" signifies a 1-center vacant orbital, "BD" abbreviates 2-center bonding (σ) orbital, and "BD*" represents a 2-center antibonding σ* orbital. (The labelling of atoms of NIF33 and MoNIF33 system has been taken from Figure 5.14.)

System	Donor NBO	Acceptor NBO	$E^{(2)}$(kcal/mol)
NIF33	BD(Fe_2-O_γ)	LP*(Fe_3)	2.81
	BD(Ni_1-O_δ)	BD*(Fe_3-O_μ)	0.62
	LP(Fe_3)	LP*(O_μ)	0.81

MoNIF33	BD(Fe_2-O_γ)	LP*(Mo_1)	12.29
	BD(Ni_1-O_δ)	LP*(Mo_1)	14.28
	BD(O_β-Mo)	LP*(O_μ)	33.85
	BD*(Fe_1-O_β)	LP*(Mo_1)	43.39

Table 5.7 shows the charge transfers (with significant interaction energy) in NIF33 and MoNIF33 systems. In NIF33 system, charge transfer occur from BD(Fe_2-O_γ) to LP*(Fe_3) NBO with 2.81 kcal/mol stabilization energy ($E^{(2)}$). Similarly, charge transfer takes place from BD(Ni_1-O_δ) to BD*(Fe_3-O_μ) with 0.62 kcal/mol $E^{(2)}$ value. Simultaneously, charge transfer from LP(Fe_3) to LP*(O_μ) NBO was observed with 0.81 kcal/mol.

In MoNIF33 system, comparatively strong charge transfer or delocalization takes place. For instance, charge transfer from BD(Fe_2-O_γ) and BD(Ni_1-O_δ) to LP*(Mo_1) occur with 12.29 and 14.28 kcal/mol stabilization energies. Another charge dispersal is from BD(O_β-Mo) to LP*(O_μ) with 33.85 kcal/mol $E^{(2)}$ value. A BD*(Fe_1-O_β) to LP*(Mo_1) interaction also occurs with 43.39 kcal/mol delocalization energy. Due to the presence of Mo atom, charge dispersals occur with significantly higher $E^{(2)}$ values. This confirms that Mo doping redistributes the charge density over the different MoNIF33 sites. The dopant Mo, substituting octahedral Fe, is significantly more electronegative than the adjacent tetrahedral Fe and octahedral Ni. This results in charge transfer from tetrahedral Fe and octahedral Ni to the Mo. The doped Mo then redistributes the charge through a delocalization process to different oxygens coordinated to it. Overall, this delocalization results in three adsorbent sites; one is Mo site, the tetrahedral Fe site and the oxygens coordinated to the Mo atom.

Thereafter, the interaction of individual CIP and MG molecules with the NIF33 and MoNIF33 clusters were calculated. The CIP molecule was kept near the different metal sites present in the MoNIF33 cluster. Moreover, different interaction energy calculations were run for the -F, -COOH groups of the CIP molecule pointing towards a particular metal center. Similarly, interaction energy calculations were run for the azo group and SO_3H group of MG molecule pointing towards various metal centres in MoNIF33 cluster. Figure 5.15(a-d) shows the most stable confirmations for the interaction of CIP with MoNIF33 system. In Figure 5.15a and 5.15b, the hydrogen of the carboxylic acid group of CIP interacts with surface hydroxyl oxygen of MoNIF33 (denoted by COOH_CIP_MoNIF33). The O (coordinated to Mo in MoNIF33)- H(CIP) and O(CIP)- H(MoNIF33) interaction distances are 1.44 Å and 1.48 Å, indicating hydrogen bond formation. Figure 5.15c and 5.15d shows that the -F atom of CIP interacts with Fe(Td). The former also has a hydrogen bond-like interaction with the H of the hydroxyl group coordinated to Fe(Td) (denoted by F_CIP_MoNIF33 model). The H (MoNIF33) - F(CIP) and Fe (MoNIF33) - F(CIP) interaction distances were 1.23 and 1.86 Å in F_CIP_MoNIF33 calculated model system.

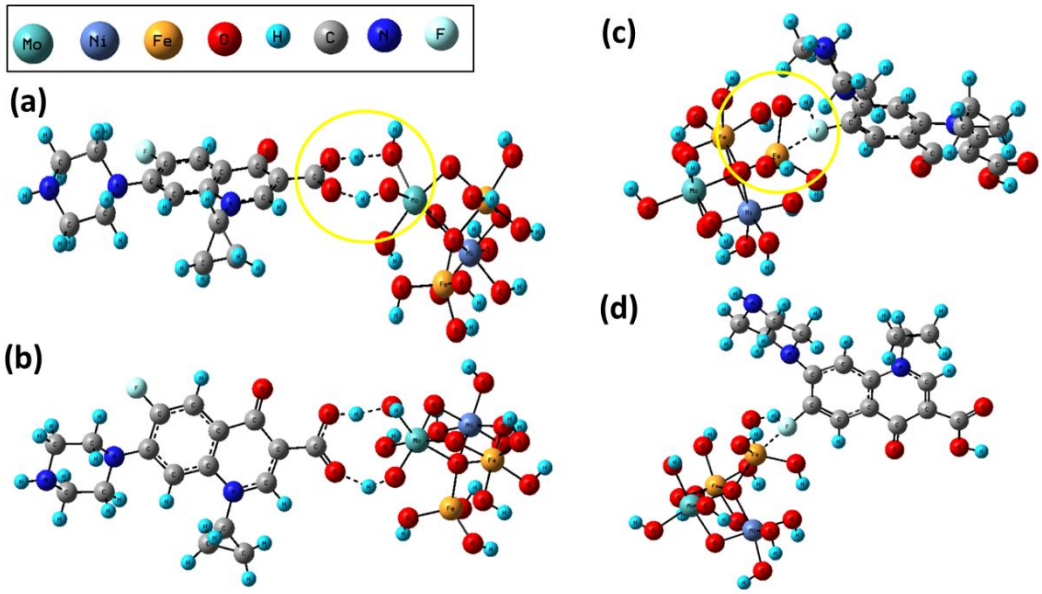

Figure 5.15 The optimized structure of, (a, b) COOH_CIP_MoNIF33 system (front and side view), (c, d) F_CIP_MoNIF33 system.

Figure 5.16a, and 5.16b show that MG interacts with the MoNIF33 cluster in two ways (denoted by S_MG_MoNIF33 system). One of them is the Mo (MoNIF33)- S(MG) interaction. The other interaction is between the hydrogen of the hydroxyl bonded to Mo and the sulphonic oxygen of MG. This interaction distance points to hydrogen formation. Figure 5.16c shows that azo group of MG molecule interacts with -OH group of MoNIF33 cluster (abbreviated as AZO_MG_MoNIF33 system).

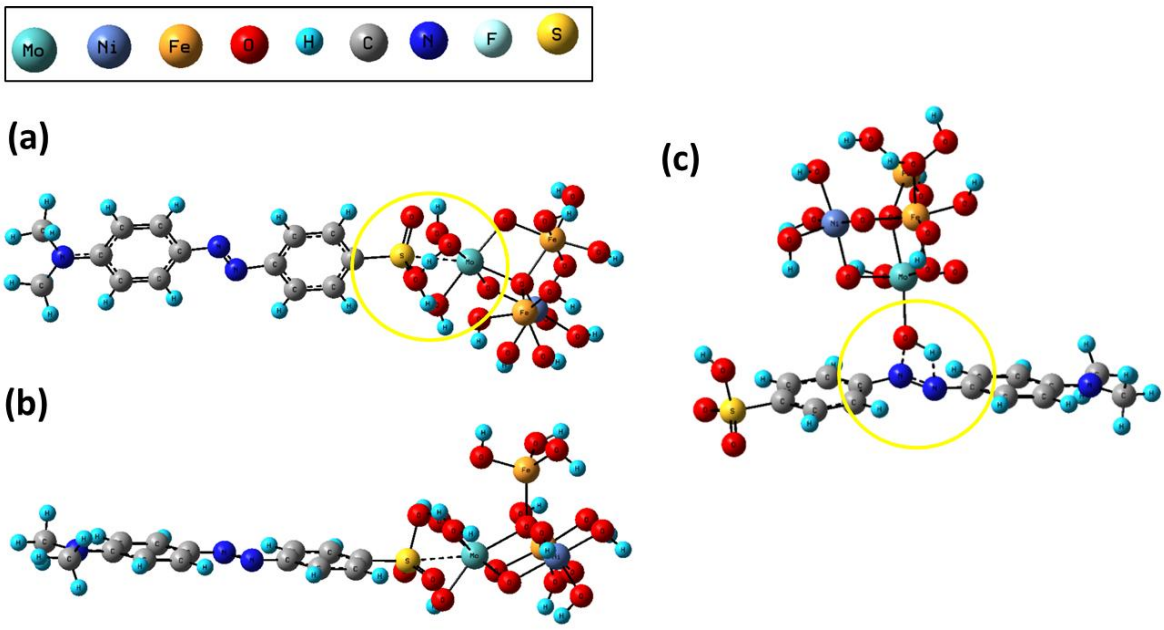

Figure 5.16 The optimized structure of, (a, b) S_MG_MoNIF33 system (front and side view), (c) AZO_MG_MoNIF33 system.

Similarly, Fig. 5.17 (a-d) shows the most stable conformations of COOH_CIP_NIF33, F_CIP_NIF33, AZO_MG_NIF33, and S_MG_NIF33 interaction systems. The COOH_CIP_NIF33 and F_CIP_NIF33 models depict CIP interaction with NIF33 through its -COOH and -F functional group, respectively. Similarly, in AZO_MG_NIF33 and S_MG_NIF33 systems, MG molecule interacts with NIF33 through azo and sulfonic group,

respectively. Table 5.8 displays the CIP and MG interaction energies with NIF33 clusters in different orientations.

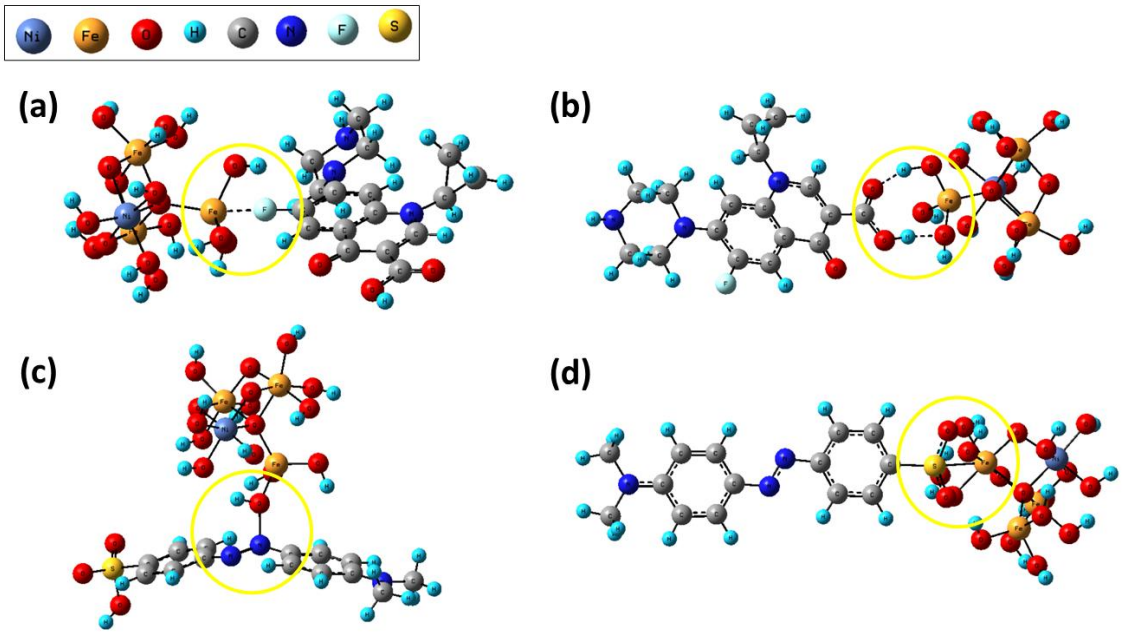

Figure 5.17 The optimized conformation of (a) F_CIP_NIF33, (b) COOH_CIP_NIF33, (c) AZO_MG_NIF33, and (d) S_MG_NIF33 systems.

The interaction energies of CIP and MG with the NIF33 and MoNIF33 system have been investigated. The interaction energies of CIP_NIF33, MG_NIF33, CIP_MoNIF33, and MG_MoNIF33 systems have been calculated using equations 5.10 to 5.13.

$$(E_{interaction})_{CIP\_NIF33} = E_{(CIP\_NIF33)} - [\, E_{(NIF33)} + E_{(CIP)}] \quad (5.10)$$

$$(E_{interaction})_{MG\_NIF33} = E_{(MG\_NIF33)} - [\, E_{(NIF33)} + E_{(MG)}] \quad (5.11)$$

$$(E_{interaction})_{CIP\_MoNIF33} = E_{(CIP\_MoNIF33)} - [\, E_{(MoNIF33)} + E_{(CIP)}] \quad (5.12)$$

$$(E_{interaction})_{MG\_MoNIF33} = E_{(MG\_MoNIF33)} - [\, E_{(MoNIF33)} + E_{(MG)}] \quad (5.13)$$

In equations 5.10 to 5.13, '$E_{interaction}$' represents the potential energy of the respective molecular system.

Table 5.8 presents the potential energies of adsorbent, adsorbate and adsorbent-adsorbate interaction models. (Note, 1 Hartree = 27.21eV)

System	Potential energy (Hartree)	Interaction energy (Hartree)
CIP	-1148.53	
MG	-1330.60	
NIF33	-6509.28	
MoNIF33	-9223.04	
F_CIP_NIF33	-7657.68	0.13
COOH_CIP_NIF33	-7657.69	0.12
S_MG_NIF33	-7838.71	1.17
AZO_MG_NIF33	-7839.80	0.08
F_CIP_MoNIF33	-10371.66	-0.10
COOH_CIP_MoNIF33	-10371.68	-0.12
S_MG_MoNIF33	-10553.71	-0.07
AZO_MG_MoNIF33	-10553.72	-0.08

Interaction energies of CIP and MG molecules with the NIF33 cluster mostly have positive values. Contrary to this, in general, the different CIP and MG interaction energies with MoNIF33 clusters have negative values (table 5.8). The adsorption of both CIP and MG molecules occurs strongly over the surface of Mo doped $NiFe_2O_4$ adsorbent compare to that on the $NiFe_2O_4$ surface. Overall, the driving force for the adsorption of CIP and MG molecules by MoNIF33 is mainly the hydrogen bond formation and electrostatic interactions.

5.4 Conclusions

$NiFe_2O_4$ nanoparticles with different Mo-doping (1, 2, and 4) percentages were prepared by a hydrothermal synthesis protocol. An analysis of the XRD patterns of these Mo-doped samples showed the formation of only the inverse spinel $NiFe_2O_4$ phase with a slight shifting of the peaks to higher 2θ values. The expansion of the $NiFe_2O_4$ lattice parameter after Mo-doping, pointed to Mo substituting Fe in the octahedral positions. DFT calculations also show that the Mo-dopant substituting the Fe in the octahedral position of the $NiFe_2O_4$ lattice model gives the most stable structure. NBO calculations indicate the more electronegative Mo substituting octahedral Fe results in three adsorbent sites; one is Mo site, the tetrahedral Fe site and the oxygens coordinated to the Mo atom. Similarly, XPS results showed that Mo doping makes the Ni and Fe positions slightly more positive and the lattice and hydroxyl oxygen sites more negative. Besides this, the BET surface area of the 1% Mo-doped $NiFe_2O_4$ increased by almost 40% compared to that of $NiFe_2O_4$ nanoparticles.

The 1% Mo-doped $NiFe_2O_4$ nanoparticles exhibited the best adsorption capacities of CIP and MG from their aqueous solutions. These adsorption capacities were 5 to 6 times higher than the values observed for co-adsorption on $NiFe_2O_4$ nanoparticles. All adsorption experiments were carried out at near neutral pH conditions. Equilibrium adsorption capacity data were evaluated for aqueous solutions with different CIP and MG concentration under isothermal conditions. The data was fitted to extended Langmuir, extended Langmuir-Freundlich, and extended Freundlich isotherms. The data best fitted the extended Freundlich isotherm model, which is consistent with the heterogeneous sites on Mo-doped $NiFe_2O_4$ nanoparticles. DFT calculations showed that COOH (CIP) and azo (MG) groups interact with the hydroxyl group coordinated to Mo, a common site for both adsorbates. The F of CIP interacts with Fe(Td) and also forms hydrogen bond with hydroxyl hydrogen coordinated to Fe(Td). At the same time, the sulfonic S interacts with Mo and

there is also a hydrogen bond like interaction between $O(SO_3H)$ and hydroxyl hydrogen coordinated to Mo.